UNIVERSITY OF BIRMINGHAM

Research at Birmingham

Nonlinear interaction between underwater explosion bubble and structure based on fully coupled model
zhang, aman; Wu, WB; Liu, YL; Wang, Qian

Document Version
Publisher's PDF, also known as Version of record

Link to publication on Research at Birmingham portal

Nonlinear interaction between underwater explosion bubble and structure based on fully coupled model

A. M. Zhang, W. B. Wu, Y. L. Liu, and Q. X. Wang

Articles you may be interested in

Experimental and numerical study on bubble-sphere interaction near a rigid wall
Physics of Fluids **29**, 092102 (2017); 10.1063/1.4993800

Experimental and numerical investigation on bubble dynamics near a free surface and a circular opening of plate
Physics of Fluids **29**, 107102 (2017); 10.1063/1.4999406

Viscous decay of nonlinear oscillations of a spherical bubble at large Reynolds number
Physics of Fluids **29**, 082112 (2017); 10.1063/1.4999940

Why do we live for much less than 100 years? A fluid mechanics view and approach
Physics of Fluids **29**, 081903 (2017); 10.1063/1.4998717

Small-charge underwater explosion bubble experiments under various boundary conditions
Physics of Fluids **28**, 117103 (2016); 10.1063/1.4967700

Numerical analysis of the jet stage of bubble near a solid wall using a front tracking method
Physics of Fluids **29**, 012105 (2017); 10.1063/1.4974073

Nonlinear interaction between underwater explosion bubble and structure based on fully coupled model

A. M. Zhang,[1,a)] W. B. Wu,[1] Y. L. Liu,[1] and Q. X. Wang[2]
[1]*College of Shipbuilding Engineering, Harbin Engineering University, 145 Nantong Street, Harbin, China*
[2]*School of Mathematics, University of Birmingham, Edgbaston, Birmingham, United Kingdom*

The interaction between an underwater explosion bubble and an elastic-plastic structure is a complex transient process, accompanying violent bubble collapsing, jet impact, penetration through the bubble, and large structural deformation. In the present study, the bubble dynamics are modeled using the boundary element method and the nonlinear transient structural response is modeled using the explicit finite element method. A new fully coupled 3D model is established through coupling the equations for the state variables of the fluid and structure and solving them as a set of coupled linear algebra equations. Based on the acceleration potential theory, the mutual dependence between the hydrodynamic load and the structural motion is decoupled. The pressure distribution in the flow field is calculated with the Bernoulli equation, where the partial derivative of the velocity potential in time is calculated using the boundary integral method to avoid numerical instabilities. To validate the present fully coupled model, the experiments of small-scale underwater explosion near a stiffened plate are carried out. High-speed imaging is used to capture the bubble behaviors and strain gauges are used to measure the strain response. The numerical results correspond well with the experimental data, in terms of bubble shapes and structural strain response. By both the loosely coupled model and the fully coupled model, the interaction between a bubble and a hollow spherical shell is studied. The bubble patterns vary with different parameters. When the fully coupled model and the loosely coupled model are advanced with the same time step, the error caused by the loosely coupled model becomes larger with the coupling effect becoming stronger. The fully coupled model is more stable than the loosely coupled model. Besides, the influences of the internal fluid on the dynamic response of the spherical shell are studied. At last, the case that the bubble interacts with an air-backed stiffened plate is simulated. The associated interesting physical phenomenon is obtained and expounded. *Published by AIP Publishing.* [http://dx.doi.org/10.1063/1.4999478]

I. INTRODUCTION

The underwater explosion is a complex physical phenomenon, which mainly includes shock wave, bubble pulsation, and liquid jet impact. To date, researchers have carried out plentiful study on the shock wave (Liang and Tai, 2006; Sprague and Geers, 2006; Kim and Shin, 2008; Brett and Yiannakopolous, 2008; Ming *et al.*, 2016; and Zhang *et al.*, 2017), and the interaction between a bubble and an elastic-plastic structure has been studied gradually (Klaseboer *et al.*, 2005; Li *et al.*, 2013; Hsiao *et al.*, 2014; Hsiao and Chahine, 2015; and Zong *et al.*, 2015). Because the underwater explosion bubble moves violently, the nearby structure will become plastic deformation. Meanwhile, the structural response changes the boundary condition and influences the dynamic behaviors of the bubble. Thus, the interaction between a bubble and a structure becomes strong nonlinear coupling effects. The nonlinear effects must be considered, which are essential to the survivability of naval ships and submarines.

On the basis of the spherical bubble model and elastic-plastic beam theory, the influence of spherical bubble pulse loads on a ship hull was studied. Hicks (1986) studied the "whipping response" of the ship hull subjected to the underwater explosion bubble. The dynamic hydro-elastic-plastic response of the ship hull induced to a bubble impulsive pressure was studied by Zong (2005) and Zhang and Zong (2012). However, spherical bubble pulsation models cannot consider the jet load that is crucial in near-field underwater explosions. In order to obtain the accurate bubble load, it is necessary to simulate the bubble dynamics with numerical methods.

Based on the potential flow theory, the boundary element method (BEM) has been widely employed to simulate the bubble dynamics. It has successfully solved the interaction between a bubble and a free surface or a rigid fixed wall (Blake and Gibson, 1981; Wang *et al.*, 1996; Wang and Khoo, 2004; Klaseboer *et al.*, 2005; Zhang and Liu, 2015; Zhang *et al.*, 2015; Liu *et al.*, 2016b; and Liu *et al.*, 2017). But the interaction between a bubble and a movable or deformable boundary has not been studied in depth. The background of using the BEM to solve the fluid-structure interaction problem mainly focuses on the wave-body interaction. Many methods, such as the mode decomposition method (Vinje and Brevig, 1981 and Koo and Kim, 2004), auxiliary function method (Wu and Hu, 2004), and acceleration

a)Author to whom correspondence should be addressed: zhangaman@ hrbeu.edu.cn

potential method (Tanizawa, 1995), have been presented to solve the hydrodynamic load on the wet surface accurately, and these theories form the basis for the fully coupled interaction. The nonlinear interaction between a bubble and a rigid movable structure has been studied (Duncan *et al.*, 1996; Chahine *et al.*, 2003; Li *et al.*, 2013; and Li *et al.*, 2016). The bubble dynamic behaviors near an elastic material are studied by Klaseboer and Khoo (2004) and Turangan *et al.* (2006). Recently, some researchers have employed the BEM combined with the finite element method to study the interaction between a bubble and an elastic-plastic structure (Klaseboer *et al.*, 2005; Li *et al.*, 2013; Hsiao *et al.*, 2014; Hsiao and Chahine, 2015; and Zong *et al.*, 2015).

The loosely coupled model is popular among the research on the interaction between the bubble and the structure because it is easy to code by means of the commercial finite element structure solver. But the non-simultaneous interaction causes the inaccuracy of the loosely coupled model. The accuracy of the modeling of the interaction between the bubble and structure relies on the precision of the bubble load. In other words, the partial derivative of the potential with respect to time ϕ_t on the wet surface needs to be solved accurately. But, solving ϕ_t by the simple finite difference method can lead to numerical instability and loss of accuracy, when the time step is very small. Besides, in order to obtain reliable prediction of loads on the wet surface, the fluid and structure control equations are needed to be solved simultaneously. However, to the best of the authors' knowledge, there are few papers expounding the theory of solving the fully coupled interaction between a bubble and an elastic-plastic structure. Besides, for underwater explosion experiments, few papers (Klaseboer *et al.*, 2005 and Brett and Yiannakopolous, 2008) focus on the structural response and bubble dynamic behaviors together.

In this paper, the fully coupled interaction between the bubble and the elastic-plastic structure is studied. The bubble dynamics are solved by the BEM, and the structural nonlinear transient response is solved by the explicit finite element method (EFEM). A new fully coupled 3D model is established through coupling the equations for the state variables of the fluid and structure and solving them as a set of coupled linear algebra equations. Based on the acceleration potential theory, the mutual dependence between the hydrodynamic load and the structural motion is decoupled. The pressure distribution in the flow field is calculated by using the Bernoulli equation, where the partial derivative of the velocity potential in time is calculated using the BIM model to avoid numerical instabilities. Because the shock wave lasts very short compared with the bubble pulsation period and the inertia of the structure is very large, it is reasonable that the structural response to the shock wave is neglected in the numerical model (Klaseboer *et al.*, 2005 and Hsiao and Chahine, 2015). The convergence study of the new model is conducted. In order to verify our numerical model, two cases of small-scale underwater explosion experiments are carried out to observe the interaction between a bubble and a submerged elastic-plastic stiffened plate. In the experiments, measurements of strain are combined with the high-speed imaging to observe the bubble-structure interaction. The numerical results are compared with the

experimental data qualitatively and quantitatively, concerning the structural strain response and bubble shapes. By both the loosely coupled model and the fully coupled model, the interactions between a bubble and a hollow spherical shell are simulated in three cases. We compare the two models to show and analyze the differences between them. Besides, the interaction between a bubble and a spherical shell filled with water is also studied. The influences of the internal fluid on the structural dynamic response are studied. Finally, in the presence of the free surface, the interaction between a bubble and an air-backed plate is simulated.

II. THEORETICAL MODEL AND NUMERICAL METHOD

A. Bubble dynamics model

A high pressure bubble will form in water after the explosive detonates. Afterwards, the bubble expands and collapses, interacting with its nearby structure. A Cartesian coordinate system *O-xyz* is built with the origin at the initial center of the bubble and the *z*-axis along the opposite direction of the gravity. For the underwater explosion bubble, the Reynolds number is high. The viscosity of the fluid can be neglected (Klaseboer *et al.*, 2005; Hsiao and Chahine, 2015; and Zhang and Liu, 2015). The fluid around the bubble is assumed to be incompressible, and the velocity potential satisfies the boundary integral equation,

$$\alpha(\boldsymbol{r})\phi(\boldsymbol{r}) = \int_S \left(\frac{\partial \phi(\boldsymbol{q})}{\partial n} G(\boldsymbol{r},\boldsymbol{q}) - \phi(\boldsymbol{q}) \frac{\partial G(\boldsymbol{r},\boldsymbol{q})}{\partial n} \right) \mathrm{d}S, \quad (1)$$

where $\boldsymbol{r}$ is the field point, $\boldsymbol{q}$ is the source point, $\boldsymbol{n}$ is the unit normal vector of the boundary, and $\alpha(\boldsymbol{r})$ is the solid angle of the point $\boldsymbol{r}$. $G(\boldsymbol{r},\boldsymbol{q}) = 1/|\boldsymbol{r}-\boldsymbol{q}|$ is the Green function. S is the surface of the fluid field, consisting of the bubble surface S_b and the wet surface of the structure S_s.

The kinematic boundary condition on the bubble surface is

$$\frac{\mathrm{d}\boldsymbol{r}}{\mathrm{d}t} = \nabla\phi \quad \text{on } S_b. \quad (2)$$

The wet surface satisfies the non-penetration condition

$$\phi_n = \dot{\boldsymbol{u}} \cdot \boldsymbol{n} \quad \text{on } S_s, \quad (3)$$

where ϕ_n is the normal derivative of ϕ and $\dot{\boldsymbol{u}}$ is the velocity of the point on the structure boundary.

The dynamic boundary condition on the bubble surface is as follows, which is obtained from the Bernoulli equation and the balance of the pressure on the surface:

$$\frac{\mathrm{d}\phi}{\mathrm{d}t} = \frac{P_\infty - P_b}{\rho_l} - gz + \frac{|\nabla\phi|^2}{2}, \quad (4)$$

where P_∞ is the hydrostatic pressure at the plane $z = 0$, P_b is the internal pressure of the bubble, ρ_l is the density of fluid, and g is the gravity acceleration.

It is assumed that the gas pressure P_b of the bubble obeys the adiabatic law (Best and Kucera, 1992),

$$P_b = P_0 \left(\frac{V_0}{V_b} \right)^\kappa, \quad (5)$$

where P_0 is the initial gas pressure of the bubble, V_0 and V_b are the initial and transient bubble volumes, respectively, and κ is the specific heat ratio, which is equal to 1.25 for the 2,4,6-trinitrotoluene (TNT) explosive (Cole, 1948). The determination of P_0 and V_0 refers to the studies of Rungsiyaphornrat *et al.* (2003) and Klaseboer *et al.* (2005).

The bubble surface and the wet surface of the structure are meshed into linear triangular elements. The boundary integral equation (1) is discretized in the block matrix form as follows:

$$\begin{bmatrix} \boldsymbol{G}_{bb} & -\boldsymbol{H}_{bs} \\ \boldsymbol{G}_{sb} & -\boldsymbol{H}_{ss} \end{bmatrix} \begin{bmatrix} \boldsymbol{\Phi}_{n,b} \\ \boldsymbol{\Phi}_s \end{bmatrix} = \begin{bmatrix} \boldsymbol{H}_{bb} & -\boldsymbol{G}_{bs} \\ \boldsymbol{H}_{sb} & -\boldsymbol{G}_{ss} \end{bmatrix} \begin{bmatrix} \boldsymbol{\Phi}_b \\ \boldsymbol{\Phi}_{n,s} \end{bmatrix}, \quad (6)$$

where $\boldsymbol{G}$ and $\boldsymbol{H}$ are the coefficient matrix, and their detailed calculation can refer to Wang (1998). The subscripts "b" and "s" are associated with the nodes on the bubble surface and the wet surface of the structure, respectively. The left-hand side of (6) contains the unknown variables: the normal velocity at the bubble surface $\boldsymbol{\Phi}_{n,b}$ and the velocity potential at the wet surface $\boldsymbol{\Phi}_s$.

On the influences of boundaries and buoyance, the bubble will form a jet at the final stage of collapse. The bubble is penetrated by the liquid jet and becomes toroidal in shape. In this paper, the vortex ring model presented by Zhang and Liu (2015) is adopted to simulate the 3D toroidal bubble.

A vortex ring is placed inside the bubble. The velocity potential can be decomposed into two parts: the potential induced by the vortex ring ϕ_i and the remainder ϕ_{res} (Wang *et al.*, 1996; 2005),

$$\phi = \phi_i + \phi_{res}. \quad (7)$$

The induced potential ϕ_i can be determined as follows (Zhang and Liu, 2015 and Liu *et al.*, 2016a):

$$\phi_i(\boldsymbol{r}) = \frac{\Gamma}{4\pi} \oint_C \left(\frac{R_z}{|\boldsymbol{R}|} \mp 1 \right) \frac{1}{R_r^2} \mathbf{e}_z \cdot (\boldsymbol{R} \times d\boldsymbol{l}), \quad (8)$$

where R_z and R_r are the component of $\boldsymbol{R}$ in the z and r directions. Γ is the strength of the vortex ring, and C is the closed curve standing for the vortex ring. "$-$" is chosen when the point $\boldsymbol{r}$ is situated above the vortex ring surface, otherwise "$+$" is chosen. According to the Biot-Savart law, the induced velocity $\nabla\phi_i$ can be obtained.

The remainder potential ϕ_{res}, which satisfies the boundary integral equation (1), is continuous in the fluid field. The dynamic boundary condition is

$$\frac{d\phi_{res}}{dt} = \frac{P_\infty - P_b}{\rho_l} - gz - \frac{|\nabla\phi|^2}{2} + \nabla\phi \cdot \nabla\phi_{res}. \quad (9)$$

The initial shape of the bubble is assumed as a sphere, whose velocity potential is zero initially. In order to ensure the stability of the numerical model, the time step in the fluid part Δt_b is set as follows (Best and Kucera, 1992):

$$\Delta t_b = R_m \sqrt{\frac{P_\infty}{\rho_l}} \frac{\Delta\phi}{\max \left| \frac{P_\infty - P_b}{\rho_l} - \frac{1}{2}|\nabla\phi|^2 - gz \right|}, \quad (10)$$

where $\Delta\phi$ is a constant, which is chosen as $\Delta\phi = 10^{-2}$ and 4×10^{-3} before and after jet impact, respectively, in order to limit the maximum changes of the velocity potential on the bubble within per time increment.

B. Structure model

Differing from the loosely coupled method, the fully coupled method requires more structural variables that are seldom provided by the commercial structure solver, such as the internal force of the nodes due to the element stress. Thus, the structure model is developed in-house in this paper. A structure nearby may undergo large transient deformation due to violent bubble dynamics, which is modeled by the explicit finite element method (EFEM) (Belytschko *et al.*, 1984), an efficient modeling for nonlinear transient dynamics for structures. According to the virtual work principle, the structural dynamic behaviors can be described,

$$-\int_\Omega \rho \ddot{\boldsymbol{u}} \cdot \delta\boldsymbol{u} d\Omega - \int_\Omega \delta\boldsymbol{\varepsilon} : \boldsymbol{\sigma} d\Omega + \int_{S_s} P\boldsymbol{n} \cdot \delta\boldsymbol{u} dS = 0, \quad (11)$$

where ρ is the mass density of the structure and $\ddot{\boldsymbol{u}}$ and $\boldsymbol{\sigma}$ are the acceleration and stress tensor at a point in the structure, respectively. P is the hydrodynamic pressure acting on the wet surface of the structure S_S. $\delta\boldsymbol{u}$ is the variation of displacement field, and $\delta\boldsymbol{\varepsilon}$ is the strain variation that is compatible with $\delta\boldsymbol{u}$. Ω is the domain of the structure.

The variable in Ω can be approximately expressed by the nodal values of the variable and shape functions (Hughes, 2000),

$$\boldsymbol{x} = \sum_{M=1}^{N_{str}} \boldsymbol{x}_M \Psi_M, \quad (12)$$

where $\boldsymbol{x}$ is the position vector in the domain of the structure, Ψ_M is the base function of node M, $\boldsymbol{x}_M$ is the spatial position of node M, and N_{str} is the total number of nodes of the domain Ω.

With the interpolation formula (12), Eq. (11) can be written in the matrix form. It can yield the explicit dynamic equation of the structural system (Hughes, 2000 and Zienkiewicz *et al.*, 2013),

$$\boldsymbol{MA} = \boldsymbol{F} - \boldsymbol{T}, \quad (13)$$

where $\boldsymbol{M}$ is the mass matrix, $\boldsymbol{A}$ is the vector of the nodal acceleration, $\boldsymbol{F}$ is the hydrodynamic load acting on the structure, and $\boldsymbol{T}$ is the nodal internal force vector due to the element stress. The components of the mass matrix $M_{MN} = \int_\Omega (\rho\Psi_M\Psi_N) d\Omega$, and the x_i-component of acceleration of node N is $A_{iN} = \ddot{u}_{iN}$. The x_i-components of external force and internal force of node M are

$$F_{iM} = \int_S \Psi_M P n_i dS, \quad (14)$$

$$T_{iM} = \int_\Omega \left(\sigma_{ij} \frac{\partial\Psi_M}{\partial x_j} \right) d\Omega. \quad (15)$$

By solving Eq. (13), the nodal acceleration can be calculated directly.

The acceleration $\ddot{\boldsymbol{u}}$ is integrated explicitly from time step n to time step $n+1$ to update the velocity $\dot{\boldsymbol{u}}$ and displacement $\boldsymbol{u}$, using the central difference scheme (Hughes, 2000 and Zienkiewicz *et al.*, 2013),

$$\dot{\boldsymbol{u}}^{n+1/2} = \dot{\boldsymbol{u}}^{n-1/2} + \ddot{\boldsymbol{u}}^n \Delta t_s^{n+1/2}, \tag{16}$$

$$\boldsymbol{u}^{n+1} = \boldsymbol{u}^n + \dot{\boldsymbol{u}}^{n+1/2} \Delta t_s^{n+1}, \tag{17}$$

where $\Delta t_s^{n+1/2} = \frac{1}{2}\left(\Delta t_s^n + \Delta t_s^{n+1}\right)$.

In this paper, our research structural object is a stiffened plate and a spherical shell, respectively. All the structural models, including the bottom plating and stiffeners, are discretized into linear triangle shell elements that share nodes with the wet surface. This avoids the interpolation of variables and the data thus can be transferred conveniently between the modelings of the fluid and structure.

Based on the Reissner-Mindlin plate theory, the shell elements have considered the transverse shear. The velocity-strain formula is

$$\dot{\varepsilon}_{ij} = \frac{1}{2}\left(\frac{\partial \dot{u}_i}{\partial x_j} + \frac{\partial \dot{u}_j}{\partial x_i}\right). \tag{18}$$

The velocity-strain $\dot{\varepsilon}_{ij}$ can be directly used in the constitutive model to update the stress $\boldsymbol{\sigma}$ [see the work of Belytschko *et al.* (1984) for details].

The EFEM is stable as the time step Δt_s satisfies (Belytschko, 1976 and Flanagan and Belytschko, 1981)

$$\Delta t_s \leq \frac{l_e}{c}, \tag{19}$$

where the characteristic length l_e is $l_e = 2A/L$, with A and L being the area and the length of the longest edge of the triangular element. The dilatational wave speed c is $c = \sqrt{E/\rho(1-v^2)}$, where E is Young's modulus and v is the Poisson ratio of the structure (Belytschko *et al.*, 1984).

C. Bubble-structure interaction model

In order to simulate the bubble-structure interaction, the hydrodynamic load must be calculated accurately. In other words, it is necessary to solve the partial derivative of the potential with respect to time ϕ_t on the wet surface accurately and stably. Adopting the backward finite difference approximation to calculate ϕ_t is not sufficiently accurate and easily causes numerical instability, especially when the time step is very small. To avoid the above problems, ϕ_t is got by solving the boundary integral equation in this paper. A 3D curvilinear coordinate system with a direct local basis $(\boldsymbol{p}, \boldsymbol{s}, \boldsymbol{n})$ is built at each node on the wet surface, where $\boldsymbol{n}$ points outside of the fluid domain.

ϕ_t on the fluid field boundary satisfies the boundary integral equation,

$$\alpha(\boldsymbol{r})\phi_t(\boldsymbol{r}) = \int\limits_S \left(\frac{\partial \phi_t}{\partial n}(\boldsymbol{q})G(\boldsymbol{r},\boldsymbol{q}) - \phi_t(\boldsymbol{q})\frac{\partial G(\boldsymbol{r},\boldsymbol{q})}{\partial n}\right)\mathrm{d}S. \tag{20}$$

The boundary condition for ϕ_t on the bubble surface can be obtained from the Bernoulli equation as follows:

$$\phi_t = \frac{P_\infty - P_b}{\rho} - gz - \frac{|\nabla\phi|^2}{2} \quad \text{on } S_b. \tag{21}$$

According to the acceleration potential theory, the boundary condition on the wet surface of the body can be obtained from the non-penetration condition (Van Daalen, 1993 and Tanizawa, 1995),

$$\phi_{tn} = \ddot{\boldsymbol{u}} \cdot \boldsymbol{n} + v \quad \text{on } S_s, \tag{22}$$

where $v = v(\boldsymbol{r}, t)$ is a function of the velocity of a solid particle at the structure boundary,

$$v = \left(\dot{\boldsymbol{u}} \cdot \boldsymbol{p} - \frac{\partial\phi}{\partial p}\right)\dot{\boldsymbol{\theta}} \cdot \boldsymbol{s} - \left(\dot{\boldsymbol{u}} \cdot \boldsymbol{s} - \frac{\partial\phi}{\partial s}\right)\dot{\boldsymbol{\theta}} \cdot \boldsymbol{p}$$
$$- \left(\frac{1}{R_p}\frac{\partial\phi}{\partial p} + \frac{\partial^2\phi}{\partial p\partial n}\right)\dot{\boldsymbol{u}} \cdot \boldsymbol{p} - \left(\frac{1}{R_s}\frac{\partial\phi}{\partial s} + \frac{\partial^2\phi}{\partial s\partial n}\right)\dot{\boldsymbol{u}} \cdot \boldsymbol{s}$$
$$+ \left(\frac{\partial^2\phi}{\partial p^2} + \frac{\partial^2\phi}{\partial s^2} - \left(\frac{1}{R_p} + \frac{1}{R_s}\right)\phi_n\right)\dot{\boldsymbol{u}} \cdot \boldsymbol{n}, \tag{23}$$

where $(\boldsymbol{p}, \boldsymbol{s}, \boldsymbol{n})$ is the local coordinates with $\boldsymbol{p}, \boldsymbol{s}$ being the two tangential directions, R_p and R_s are the radii of curvature of the wet surface boundary, respectively, and $\dot{\boldsymbol{u}}$ and $\dot{\boldsymbol{\theta}}$ are the translation velocity and the rotation angular velocity of the solid particle, respectively.

It can be seen from (22) that ϕ_t and the hydrodynamic load depend on the structural deformation. Meanwhile, the structural deformation in turn depends on the hydrodynamic load. Therefore, the fluid flow and the structural motion are fully coupled. Both ϕ_t and ϕ_{tn} on the wet surface depending on $\ddot{\boldsymbol{u}}$ are unknown. The boundary integral equation (20) can be transformed into N discretized equations with $N + N_s$ unknowns, where N and N_s are the total numbers of the nodes on the fluid boundary and wet surface, respectively. New conditions are required to close the model.

The component format of the structural control equation (13) is

$$m_M \ddot{u}_{iM} = F_{iM} - T_{iM}, \tag{24}$$

where m_M is the lumped mass of node M, $\ddot{u}_{iM}$, F_{iM} and T_{iM} are the x_i-component of the nodal acceleration, the external loading, and the nodal internal force of the node M, respectively. With the Bernoulli equation, the hydrodynamic load F_{iM} is

$$F_{iM} = \int\limits_{S_S} \Psi_M P n_i \mathrm{d}S = \rho_l \int\limits_{S_S} \Psi_M \left(-\phi_t - \frac{1}{2}|\nabla\phi|^2\right)n_i \mathrm{d}S, \tag{25}$$

where n_i is the x_i-component of the normal vector $\boldsymbol{n}$. Note that the internal force T_{iM} contributed by the stress at the current state is obtained by (15), (18), and material models. Thus, the internal force is a known quantity.

Substituting Eqs. (24) and (25) into Eq. (22), we can yield the relationship between ϕ_{tn} and ϕ_t on the wet surface in the discretized form, applied in the node M,

$$\phi_{tn,M} + \frac{\rho_l}{m_M}\int\limits_{S_S} \Psi_M \phi_t \boldsymbol{n}\mathrm{d}S \cdot \boldsymbol{n}_M$$
$$= -\frac{\rho_l}{2m_M}\int\limits_{S_S} \Psi_M |\nabla\phi|^2 \boldsymbol{n}\mathrm{d}S \cdot \boldsymbol{n}_M - \frac{\boldsymbol{T}_M \cdot \boldsymbol{n}_M}{m_M} + v_M \quad \text{on } S_s. \tag{26}$$

The integral in the above equation is calculated on the wet surface of the structure S_S. The linear elements on the wet surface are described with two parameters (ξ, η), with vertices located at $(1, 0)$, $(0, 1)$, and $(0, 0)$ in the anti-clockwise direction. The shape functions are $\varphi_1 = \xi$, $\varphi_2 = \eta$, and $\varphi_3 = 1 - \xi - \eta$. The variable of the element can be expressed as $\phi_t = \sum_{k=1}^{3} \varphi_k \phi_{t,k} = \boldsymbol{\varphi} \cdot \boldsymbol{\phi}_t$, where $\boldsymbol{\varphi} = [\varphi_1, \varphi_2, \varphi_3]$ is the shape function matrix of the element and $\boldsymbol{\phi}_t = [\phi_{t,1}, \phi_{t,2}, \phi_{t,3}]^T$ is the vector of the variables at vertices of the element.

With the above definition, (26) can be written as

$$\phi_{tn,M} + \sum_{j=1}^{N_{surr}} \boldsymbol{C}_M^{(j)} \cdot \boldsymbol{\phi}_t^{(j)}$$
$$= - \sum_{j=1}^{N_{surr}} \frac{1}{2} \boldsymbol{C}_M^{(j)} \cdot \left| \nabla \boldsymbol{\phi}^{(j)} \right|^2 - \frac{\boldsymbol{T}_M \cdot \boldsymbol{n}_M}{m_M} + v_M \quad \text{on } S_s, \quad (27)$$

where j denotes the jth element around the node M and N_{surr} is the number of the surrounding elements around node M. The superscript (j) denotes the variable of the jth element. $\boldsymbol{C}_M^{(j)} = \frac{\rho_l}{m_M} \int_{S_j} \varphi_K \boldsymbol{n} \cdot \boldsymbol{\varphi} \, dS \cdot \boldsymbol{n}_M$, where φ_K is the component of base function $\boldsymbol{\Psi}_M$ in the jth element. The vector $\boldsymbol{C}_M^{(j)}$ means the contribution of the jth element to the node M. $\boldsymbol{C}_M^{(j)}$ only depends on the geometry of the wet surface and material properties. And it can be numerically solved by Gauss' integral identity. The right-hand side of Eq. (27) can be determined by the state of the wet surface at the current time, including the material properties, geometry, internal force, and structural and fluid motion.

The matrix form of (27) is

$$\boldsymbol{\Phi}_{tn} + \boldsymbol{C}\boldsymbol{\Phi}_t = \boldsymbol{\beta} \quad \text{on } S_s. \quad (28)$$

Based on the explicit finite element and the acceleration potential theory, the extra relationship between ϕ_t and ϕ_{tn} on the wet surface is established. Equation (28) is the implicit boundary condition of the elastic-plastic structure.

Combining (20) and (28) yields the control equation which is expressed in the block matrix form as follows:

$$\begin{bmatrix} \boldsymbol{G}_{bb} & -\boldsymbol{H}_{bs} & \boldsymbol{G}_{bs} \\ \boldsymbol{G}_{sb} & -\boldsymbol{H}_{ss} & \boldsymbol{G}_{ss} \\ \boldsymbol{0} & \boldsymbol{C} & \boldsymbol{I} \end{bmatrix} \begin{bmatrix} \boldsymbol{\Phi}_{tn,b} \\ \boldsymbol{\Phi}_{t,s} \\ \boldsymbol{\Phi}_{tn,s} \end{bmatrix} = \begin{bmatrix} \boldsymbol{H}_{bb}\boldsymbol{\Phi}_{t,b} \\ \boldsymbol{H}_{sb}\boldsymbol{\Phi}_{t,b} \\ \boldsymbol{\beta} \end{bmatrix}, \quad (29)$$

where $\boldsymbol{I}$ is the unit matrix of dimension $N_s \times N_s$. The known variables and unknown variables in (29) are arranged on the right and left sides, respectively. Equation (29) is a linear system of $N + N_s$ discretized equations with $N + N_s$ unknowns.

The time derivative of the potential on the wet surface $\boldsymbol{\Phi}_{t,s}$ can be obtained directly and accurately. Using Eq. (25), the hydrodynamic load on the wet surface can be calculated. Besides, most of the coefficient matrices in Eq. (29) have been calculated in Eq. (6). During the calculation of $\boldsymbol{\Phi}_{t,s}$, the extra computation is very little. The method can save much central processing unit (CPU) time. It deserves to be mentioned that $\ddot{\boldsymbol{u}}$ is generated under the action of the hydrodynamic pressure induced by the bubble and the added mass force caused by the structural motion. Thus, $\boldsymbol{\Phi}_{t,s}$ has included the influence of the added mass.

If the time step of the whole bubble-structure interaction system is set as $\Delta t = \min(\Delta t_s, \Delta t_b)$, computational cost is too much and it is unnecessary to update the hydrodynamic load at all times because Δt_s is very little for the EFEM. Therefore, the fluid domain and structural domain use their respective time step Δt_b and Δt_s to update their information in this paper. The leapfrog time-advancing scheme is adopted to deal with the different time steps of the fluid and structural domains (Klaseboer *et al.*, 2005). Besides, $\Delta t_b = \min(500\Delta t_s, \Delta t_b)$ in this paper. We assume that the hydrodynamic load is invariable during the time step Δt_b. When $T_s \geq T_b$, the fluid solver and the decouple solver are executed. It is worth mentioning that the structural time step is modified by $\Delta t_s^{modified} = \Delta t_s - (T_s - T_b)$ at this time. Hence, the time discrepancy between the fluid and structural parts can be eliminated, and the variables of the fluid and structural domains can be ensured at the same time. The displacement, normal velocity, internal force, and mass information of the wet surface are transferred from the structural part to the fluid part. The hydrodynamic load is calculated by using Eqs. (29) and (25), and then it is returned to the structural

FIG. 1. Flow chart of the computation procedure.

part. The flow chart of the whole bubble-structure interaction computation procedure is given in Fig. 1.

In a word, based on the acceleration potential theory, the implicit boundary condition of the elastic-plastic structure is derived, which establishes the extra relation between ϕ_t and ϕ_{tn} on the wet surface. The implicit boundary condition Eq. (28) can be added to the original boundary integral equation (20) so that the underdetermined problem is solved. It can decouple the mutual dependence between the hydrodynamic load and the structural motion. The solution of the matrix equation provides ϕ_t in the Bernoulli equation. By integrating the pressure over the wet surface, the external loading is obtained and transferred to the structural domain. The structural displacement and velocity can be updated to the next time step. The model can ensure that the pressure P and normal velocity are continuous at the fluid-structure interface.

III. EXPERIMENT

Two cases of small-scale underwater explosion experiments are carried out to observe the bubble-structure interaction. The experimental setup refers to the work of Cui *et al.* (2016b). Experiments are conducted in a 2 m × 2 m × 2 m water tank, made of 10 mm steel plate. The water tank is full of water. The charge with a weight of 4 g pentaerythritol tetranitrate (PETN), which is equivalent to 5.2 g TNT, is placed in the center of the water tank. The structure is fully submerged in the water. The high speed camera is used to record the behaviors of the bubble through the observation window. The configuration of the experimental setup is shown in Fig. 2.

The target structure is an elastic-plastic stiffened plate, which is composed of the outer bottom plating and stiffeners.
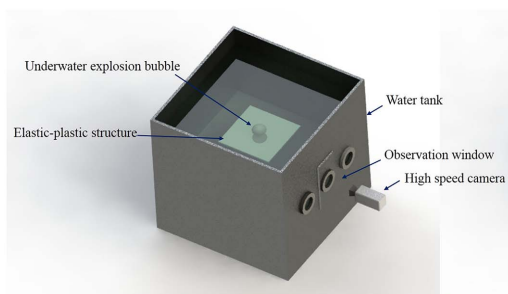
FIG. 2. Schematic of the experimental setup.

FIG. 4. Stress-strain relationships for the mild steel Q235A.

The size of the bottom plating is 1.20 m × 1.20 m, and the thickness is 2 mm. Five horizontal stiffeners and five vertical stiffeners are welded on the bottom plating. The distance of the neighboring stiffeners is 0.25 m. The stiffened plate is rigidly fixed at the corners of the bottom plating. The configuration of the stiffened plate and its size is shown in Fig. 3, where A1 and A2 denote the strain gauges. They are arranged at the corner of interior panels on the bottom plating to measure the dynamic strain in the direction of the T-section beams. The position of A1 is nearest to the position of the charge in order to measure the strain response caused by the bubble jet, and the strain gauge A2 is used to measure the strain response caused by the bubble pulsating. The stiffened plates are horizontally placed above and below the charge, respectively. Both stand-off distances are 0.19 m.

The material of the whole model is mild steel Q235A. Its material properties are as follows: Young's modulus $E = 2.03 \times 10^5$ MPa, the Poisson ratio $\upsilon = 0.30$, the density $\rho = 7800$ kg/m^3, the yield stress $\sigma_0 = 235$ MPa, and the tangent modulus $E_T = 400$ MPa. According to the bilinear elastic-plastic material hypothesis, the stress-strain relationships for the mild steel Q235A are plotted in Fig. 4.

IV. VALIDATION OF NUMERICAL MODEL

A. Convergence test

In order to prove the robustness of the new numerical model, the convergence analysis about the mesh size is

FIG. 3. Configuration of the stiffened plate and arrangement of strain gauges.
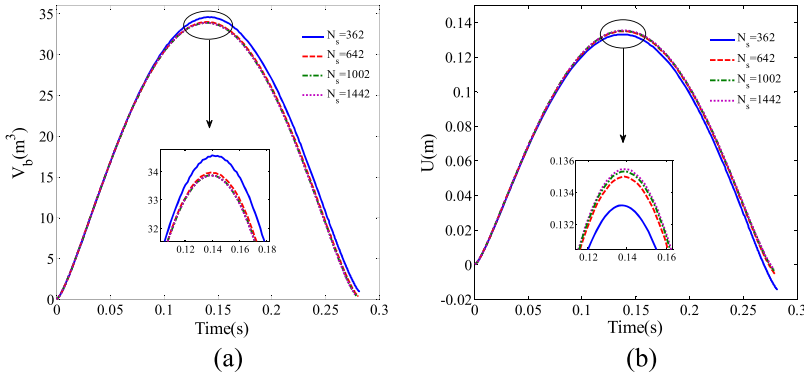
FIG. 5. Convergence study with different node numbers. (a) Time evolution of the bubble volume. (b) Time evolution of the displacement at the stand-off point.

performed in this section. An extreme case that a bubble interacts with a movable rigid sphere is considered. The weight of the TNT charge W is 4.2 kg. The depth of the charge H is 10 m. The sphere and the charge are located in the same horizontal. The distance between their centers is 4.4 m. The hollow sphere whose radius is 2 m is fully submerged in the water. When Young's modulus E tends to infinity and the Poisson ratio υ tends to zero, the structure can be regarded as a rigid body, which corresponds to a bubble near a movable rigid body. We set the material properties of the elastic sphere as follows: the mass density $\rho = 7800$ kg/m^3, Young's modulus $E = 2.1 \times 10^4$ GPa, and the Poisson ratio $\upsilon = 0$. The sphere can stay at rest in the water. According to Cole (1948), the bubble maximum radius R_m can be obtained.

The bubble and sphere surface are discretized with the same node number N_s, which equals 362, 642, 1002, and 1442, respectively. The discretization of the bubble and spherical shell is based on an icosahedron as described in the work of Wang (1998), which can ensure the high quality of mesh. Figure 5 shows the convergence study with different node numbers. Figure 5(a) shows the time evolution of the bubble volume with different node numbers. Figure 5(b) shows the time evolution of the displacement of the stand-off point (the node on the sphere which is nearest to the bubble) with different node numbers. With the node number increasing, the results tend towards the result of $N_s = 1442$ gradually. It can be seen

that the new model is shown to be convergent with the mesh size. The sphere is pushed away during the bubble expansion stage and the sphere is attracted during the bubble collapse stage.

B. Case 1

In order to validate our model, we compare the numerical results with the small-scale underwater explosion experiments. The case with the stiffened plate above the bubble is studied in this section. Figure 6 shows the bubble expansion, collapse, and jet in the first pulsation period. The numerical results in Figs. 6, 8, 10, 12, and 15 are non-dimensionalized with R_m, P_∞, and $\sqrt{P_\infty / \rho_l}$ as the length scale, pressure scale, and velocity scale. V_n of color bar represents the value of the dimensionless normal velocity. Initially, due to the interior high pressure, the bubble expands spherically and the surrounding liquid is pushed outwards, which makes four central panels deform upward and bulge slightly. Then, because of the existence of the nearby structure, the motion of the liquid between the upper part of bubble and the structure is blocked. This leads to the fact that the non-spherical characters of the bubble appear. When the bubble adheres to the bottom plate, the top of the bubble surface is flattened. At this moment, the central panels move towards the bubble, which has been observed by Klaseboer *et al.* (2005). This can be explained that the hydrodynamic load on the blast side is lower than that
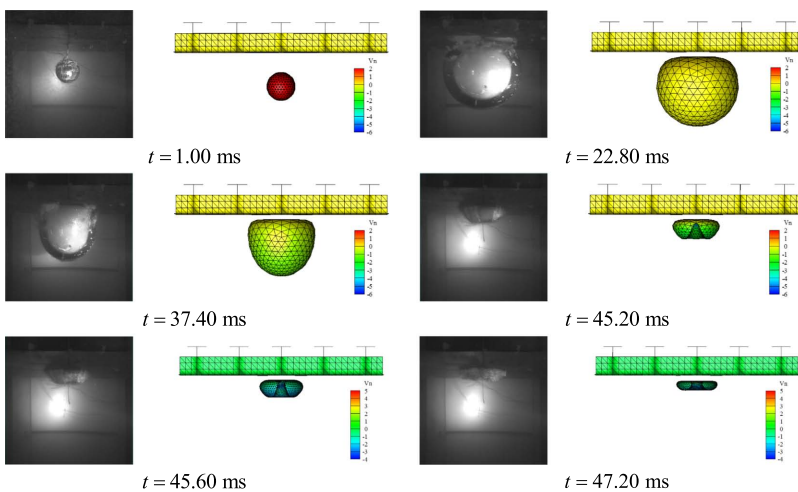

$t = 1.00$ ms

$t = 22.80$ ms

$t = 37.40$ ms

$t = 45.20$ ms

$t = 45.60$ ms

$t = 47.20$ ms

FIG. 6. Comparison between experimental (Cui *et al.*, 2016b) and numerical results of explosion below the stiffened plate. Here, $W = 5.2$ g, $H = 1$ m, and the stand-off distance is 0.19 m.

on the opposite side. Thus, the bubble has a suction effect, and the deformation of panels can be seen obviously. Afterwards, the internal pressure of the bubble is lower than the surrounding fluid pressure, and the bubble over-expands due to the inertia. Then the bubble enters the stage of collapse, and a high speed water jet is developed towards the structure under the combined action of the Bjerknes effect and the buoyancy. When the jet impacts on the opposite side of the bubble, the bubble becomes a toroidal bubble. Figure 6 (t = 45.20 ms) shows the moment that the jet penetrates the bubble surface and impinges on the structure boundary. Due to the high pressure region in the middle of the bottom plate, the central part moves upwards again. Besides, the jet splashes onto the structure boundary. It makes the bubble surface covered by the gas-liquid mixture, which is shown as the white volume in Fig. 6 (t = 47.20 ms). As shown in Fig. 6, the simulated bubble shape shows excellent agreement with the experiment (Cui *et al.*, 2016b).

The comparison of the strain response at the positions A1 and A2 between the numerical and experimental results is shown in Fig. 7. Excluding the initial short phase, the numerical results are well matched by experimental results in general. As shown in Fig. 7(a), the error of the maximum of the strain response caused by the jet is about 6.4%. According to the empirical equation in the work of Geers and Hunter (2002), we can obtain that the pulse width of the shock wave is 1.60×10^{-5} s in the experiment. The sampling time interval of the strain gauge is 2.00×10^{-7} s. Thus, the gauge can capture the high frequency response in the measured strain. However, the numerical model neglects the shock wave, and we cannot obtain the first peak caused by the shock wave in the numerical results. Besides, the reason is that the simple material model is adopted in the numerical computation, which differs from the real material.

There exist two peaks in the first pulsation period, as shown in the experimental strain curve of A1. The strain gauge A1 is situated next to the charge, where the position is subjected to the stronger underwater explosion loads. During the underwater explosion process, the large explosion load appears in the shock wave, initial bubble pulsation phase, and jet phase. Initially, due to the influence of the shock wave, the strain response rises rapidly to the first peak whose value is approximately 1650 µε, followed by a sudden drop to the value −400 µε. Then, under the action of the bubble load, the strain response rises to 450 µε. During the period

between 10 ms and 44 ms, the explosion load is extremely small compared to the prior load. And the motion of the stiffened plate can be approximately regarded as the free vibration. Because the surrounding liquid blocks the motion of the structure, it leads to the energy dissipation of the structure and the vibration amplitude of the strain response decreases gradually. At the final stage of the pulsation period, the strain at the position A1 rises rapidly when the time is approximately 45 ms. By means of the experimental imaging, we find that the time is approximately the moment that the jet impacts. It indicates that the second peak of the strain response can be attributed to the jet impacting. The position of the strain gauge A1 is in the region of the jet impacting. The water hammer pressure induced by the jet is exerted on the central region of the vortex ring, which causes damage to the structure. It can be seen that the second strain peak is comparable to the first peak in magnitude. It suggests that the jet impact load is an important factor for causing plastic deformation of small-scale structures. For the gauge A2, there is only a strain peak in the first pulsation period. Afterwards, the strain response oscillates around the value about 0 during the bubble pulsation. Zhang *et al.* (2015) analyzed the pressure field induced by a collapsing bubble near a rigid boundary. They found that the water jet load manly focuses on the central region of the vortex ring. Because the position A2 is outside the high pressure region, the strain of A2 does not change suddenly at the stage of jet. The strain response at the position A2 is approximately 80 µε at last. It means that the position of A2 does not become obvious plastic deformation in the direction of the T-section beam.

C. Case 2

In this section, the case with the stiffened plate below the bubble is studied numerically and experimentally. The dynamic behaviors of the bubble are similar to case 1. After the explosive detonates, the bubble which contains high temperature and high pressure explosive products is generated. Then, the bubble expands spherically. Because the stand-off distance is less than R_m, the bubble adheres to the structure boundary. The lower surface of the bubble is attracted by the structure due to the second Bjerknes force, while the upper surface of the bubble rises under the action of the buoyancy. With the bubble volume increasing, the inner pressure of the bubble decreases to the surrounding fluid pressure. Afterwards,
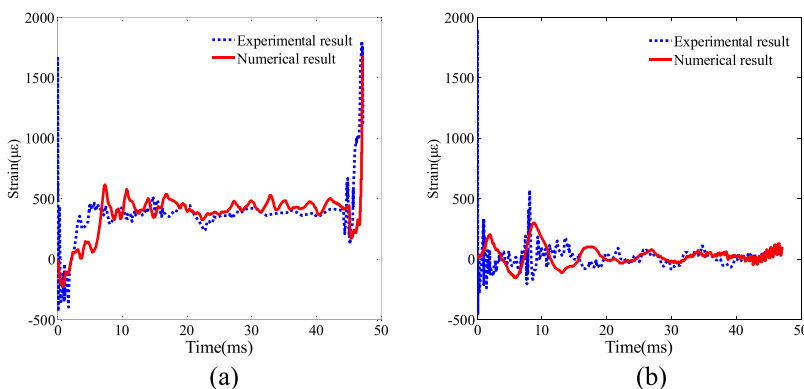

FIG. 7. Comparison of the strain response between experimental and numerical results in the direction of the T-section beam. (a) Strain curve at A1. (b) Strain curve at A2. Here, W = 5.2 g, H = 1 m, and the stand-off distance is 0.19 m.

t = 0.80 ms   t = 24.40 ms

t = 36.27 ms   t = 45.47 ms
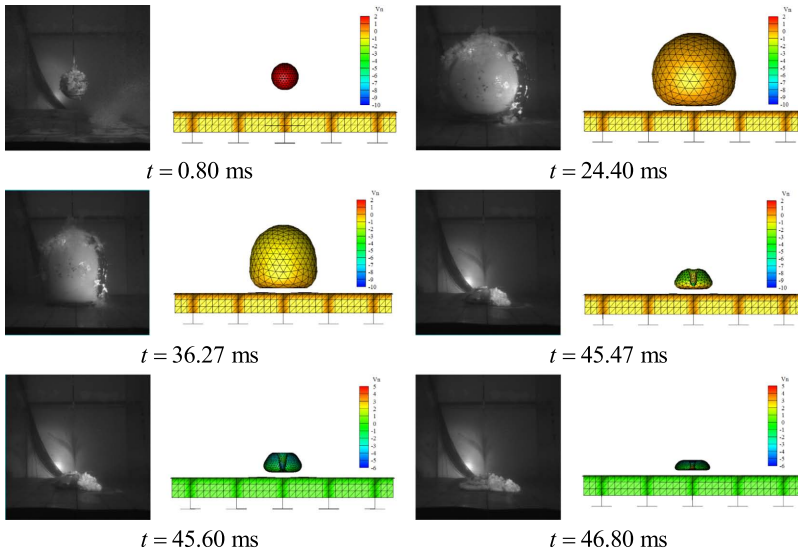
t = 45.60 ms   t = 46.80 ms

FIG. 8. Comparison between experimental and numerical results of explosion above the stiffened plate. Here, $W = 5.2$ g, $H = 1$ m, and the stand-off distance is 0.19 m.

the bubble begins to collapse. For this case, the action of the Bjerknes effect and the buoyancy on the bubble are in the opposite direction. Because the bubble radius is small in this case, the buoyancy action is not obvious. However, due to the short stand-off distance, the Bjerknes effect plays a dominant role in the bubble dynamics. It results in the conical jet directing towards the structure. Figure 8 shows the comparison of bubble dynamic behaviors between experimental and numerical results. The numerical bubble shapes correspond well with the observed experimental data, as shown in Fig. 8. In the numerical simulation, the influence of the free surface and water tank boundaries on the bubble is neglected, which may lead to the fact that the error of the maximum of the bubble radius is 9.7%. The motion law of central panels is similar to case 1 with the stiffened plate above the bubble. The central panels moves away from the bubble immediately after the denotation. Then the panels are attracted by the bubble, reverse direction, and move towards the bubble. The suction effect of the bubble can be obviously observed in Fig. 8 ($t = 36.27$ ms).

The experimental and numerical results of A1 and A2 strain responses are presented in Fig. 9. For the experimental strain response of the gauge A1, the initial shock wave generates the first strain peak immediately after the detonation. And the strain at the position A1 very rapidly decreases to

approximately −650 με. With the bubble expanding, the strain at the position A1 increases to 450 με within 6 ms under the action of liquid pushing. Then, the stiffened structure vibrates freely, and the strain response oscillates around the value about 480 με during the period from 8 ms to 43 ms. Finally, due to the jet impacting, the strain response decreases to approximately −690 με within 0.5 ms. There is a reduction in the second strain peak compared with that in case 1 because the buoyancy weakens the influence of the Bjerknes effect. The strain gauge at the position A2 measures a peak strain close to 1200 με due to the shock wave. And the position of the point A2 does not become obvious plastic deformation in the direction of the T-section beam, which is similar to case 1. Exclusion of the initial shock wave phase, the computed strain is very closer to the experimental results in general, as shown in Fig. 9.

V. NUMERICAL RESULTS AND DISCUSSIONS

A. Interaction between a bubble and a hollow spherical shell

The interaction between a bubble and an elastic-plastic hollow spherical shell is studied in this section. The weight W and initial depth H of the TNT charge are 20 g and 1 m,
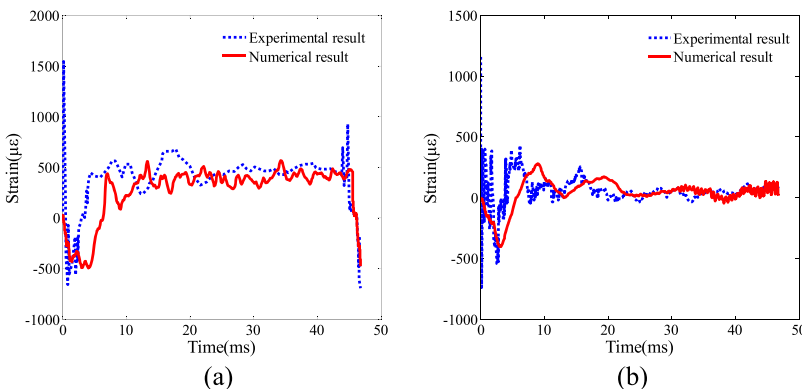

(a)

(b)

FIG. 9. Comparison of the strain response between experimental and numerical results in the direction of the T-section beam. (a) Strain curve at A1. (b) Strain curve at A2. Here, $W = 5.2$ g, $H = 1$ m, and the stand-off distance is 0.19 m.

respectively. The radius of the sphere is 0.41 m. With the different materials of the spherical shell and different distances between the bubble and sphere, the numerical results are simulated in three cases. The materials are a steel spherical shell with a thickness of 15 mm, a steel spherical shell with a

thickness of 1 mm, and an aluminum alloy spherical shell with a thickness of 1 mm, respectively. And the corresponding initial distances between the bubble center and spherical center d are 1.03 m, 1.03 m, and 0.82 m, respectively. The material of the spherical shell is mild steel
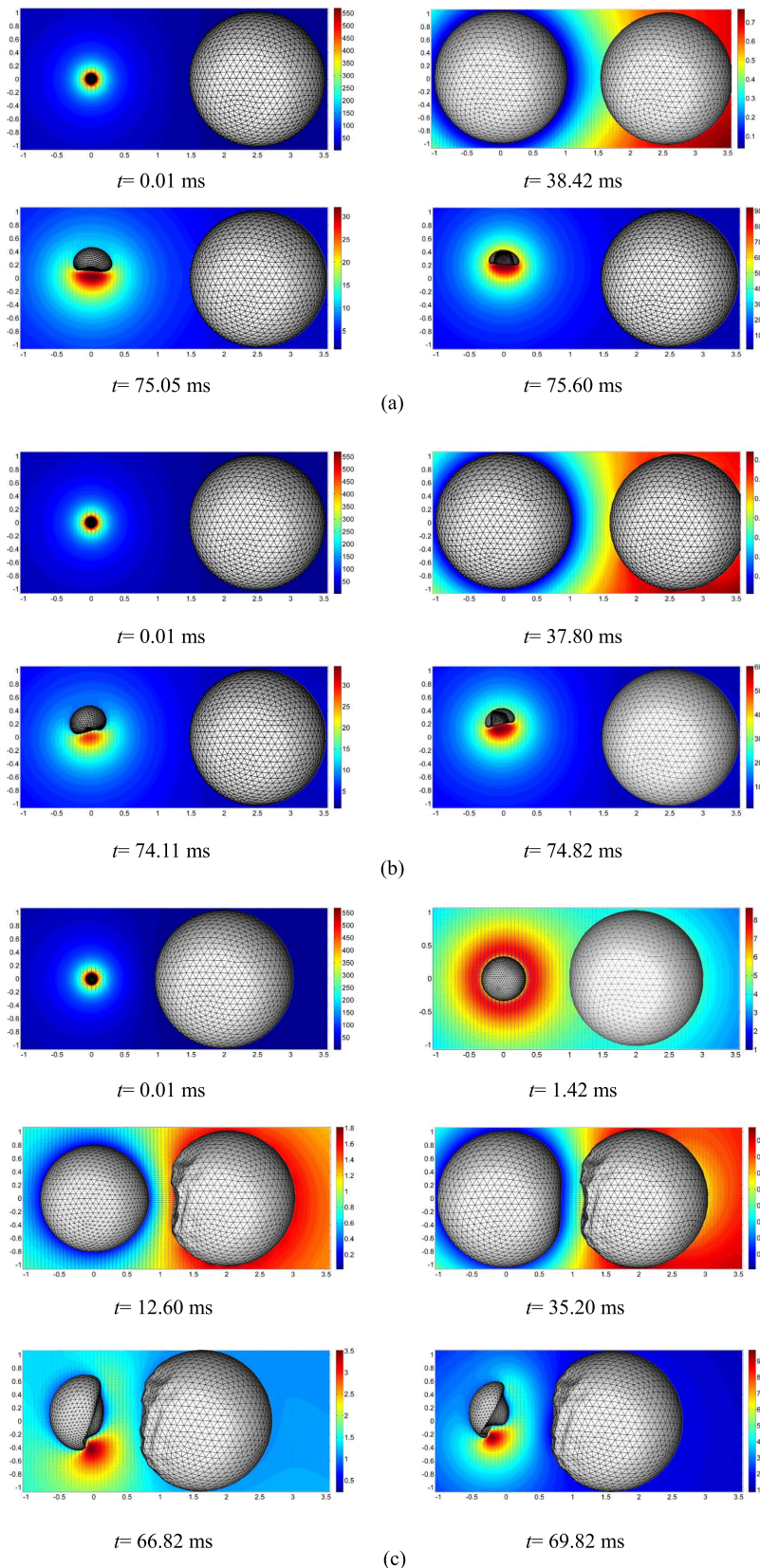
FIG. 10. Pressure contours of interactions between a bubble (left) and a sphere (right) with three different conditions: (a) a steel spherical shell with a thickness of 15 mm, $d = 1.03$ m; (b) a steel spherical shell with a thickness of 1 mm, $d = 1.03$ m; and (c) an aluminum alloy spherical shell with a thickness of 1 mm, $d = 0.82$ m. For all cases, $W = 20$ g, $H = 1$ m, and the radius of the sphere is 0.41 m.

Q235A or aluminum alloy. Their stress-strain relationships are both assumed to be the bilinear elastic-plastic material hypothesis. The material model of Q235A in Sec. III is adopted again. The material properties of the aluminum alloy are Young's modulus $E = 6.31 \times 10^4$ MPa, the Poisson ratio $\upsilon = 0.33$, the density is $\rho = 2784.5$ kg/m^3, the yield stress $\sigma_0 = 70.41$ MPa, and the tangent modulus $E_T = 1130$ MPa.

By the fully coupled model, the collapse and jet patterns of the bubble, pressure contours, and velocity fields are shown in Fig. 10. And the comparison of time histories of the displacement of the stand-off point between the loosely coupled model and fully coupled model is shown in Fig. 11. The fully coupled model and the loosely coupled model are advanced with the same time step.

Figure 10(a) displays the interaction between a bubble and a steel spherical shell with a thickness of 15 mm. Due to the material properties and thickness of the sphere, the sphere tends to a rigid structure in this case. Thus, the hydrodynamic load does not cause obvious deformation of the spherical shell. Under the combined action of the buoyancy and the Bjerknes effect of the sphere, the bubble forms a slightly oblique jet towards the sphere. The jet pattern of the bubble is similar to the case that a bubble interacts with a rigid movable sphere. It indicates that the coupling effect is weak in this case. Figure 11(a) shows the history of the displacement of the stand-off point. As Fig. 11(a) shows, there are no significant differences between the results of the loosely coupled model and the fully coupled model in this case. Because the structural response is weak and varies slightly during the whole process, the partitioned way in the loosely coupled method does not have much influence on the accuracy of the hydrodynamic load.

Figure 10(b) shows the dynamic behaviors of a bubble interacting with a steel spherical shell with a thickness of 1 mm. When the thickness of the spherical shell decreases, the stiffness of the structure decreases. Due to the existence of the elastic-plastic boundary, the high pressure region in the fluid field appears in the lower right corner of the bubble, and it makes the fluid rush into the bubble. As shown in Fig. 10(b), the wide jet develops away from the

sphere. It indicates that the effects of elastic-plastic boundary have the influence on the bubble dynamic behaviors, which differs from the Bjerknes effect of the rigid wall. Because the coupling effect becomes stronger in this case, the discrepancies between the results of the loosely coupled model and the fully coupled model become wider, as shown in Fig. 11(b). In the loosely coupled model, the hydrodynamic load is solved with the structural response in the last time step. With the stiffness of the structure decreasing, the structural response varies more obviously. Thus, the inaccuracy caused by non-simultaneous interaction in the loosely coupled model is enlarged.

Figure 10(c) displays the interaction between a bubble and an aluminum alloy spherical shell with a thickness of 1 mm. Due to the decrease of the elastic modulus of the material, the stiffness of the structure decreases again. The large bubble load causes the spherical shell bucking, as shown in Fig. 10(c) ($t = 12.60$ ms). It leads to the fact that the spherical shell becomes nonlinear large deformation. When the time reaches 35.20 ms, the bubble surface is flattened under the influence of the structure boundary. Due to the strong effects of elastic-plastic boundary, the bubble becomes mushroom-shaped afterwards, which has been observed by Klaseboer and Khoo (2004) and Turangan *et al.* (2006). In this case, the high pressure region in the fluid field appears in the bottom of the bubble, and a thin jet develops leftwards under the influence of the structure. The coupling effect is strong nonlinear in this case. In Fig. 11(c), the violent variations of the structural response cause the wide discrepancies between the results of the loosely coupled model and fully coupled model, in terms of the jet impact time and structural displacement. Thus, when the fully coupled model and the loosely coupled model are advanced with the same time step, the fully coupled model is more stable.

B. Interaction between a bubble and a spherical shell with internal fluid

In this section, the interaction between an explosion bubble and an elastic spherical shell filled with water is studied. The weight of TNT charge W is 0.4 g. The initial depths of
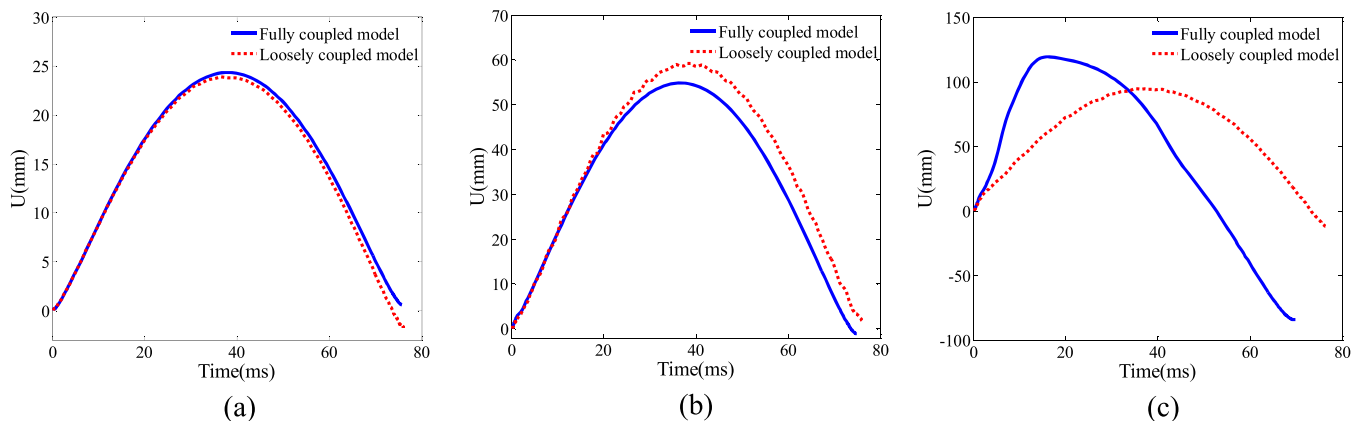

FIG. 11. Comparison of the history of the stand-off point displacement between the fully coupled model and the loosely coupled model with three different conditions: (a) a steel spherical shell with a thickness of 15 mm, $d = 1.03$ m; (b) a steel spherical shell with a thickness of 1 mm, $d = 1.03$ m; and (c) an aluminum alloy spherical shell with a thickness of 1 mm, $d = 0.82$ m. For all cases, $W = 20$ g, $H = 1$ m, and the radius of the sphere is 0.41 m.

t = 0.01 ms

t = 0.59 ms

t = 10.44 ms

t = 20.41 ms

t = 20.58 ms

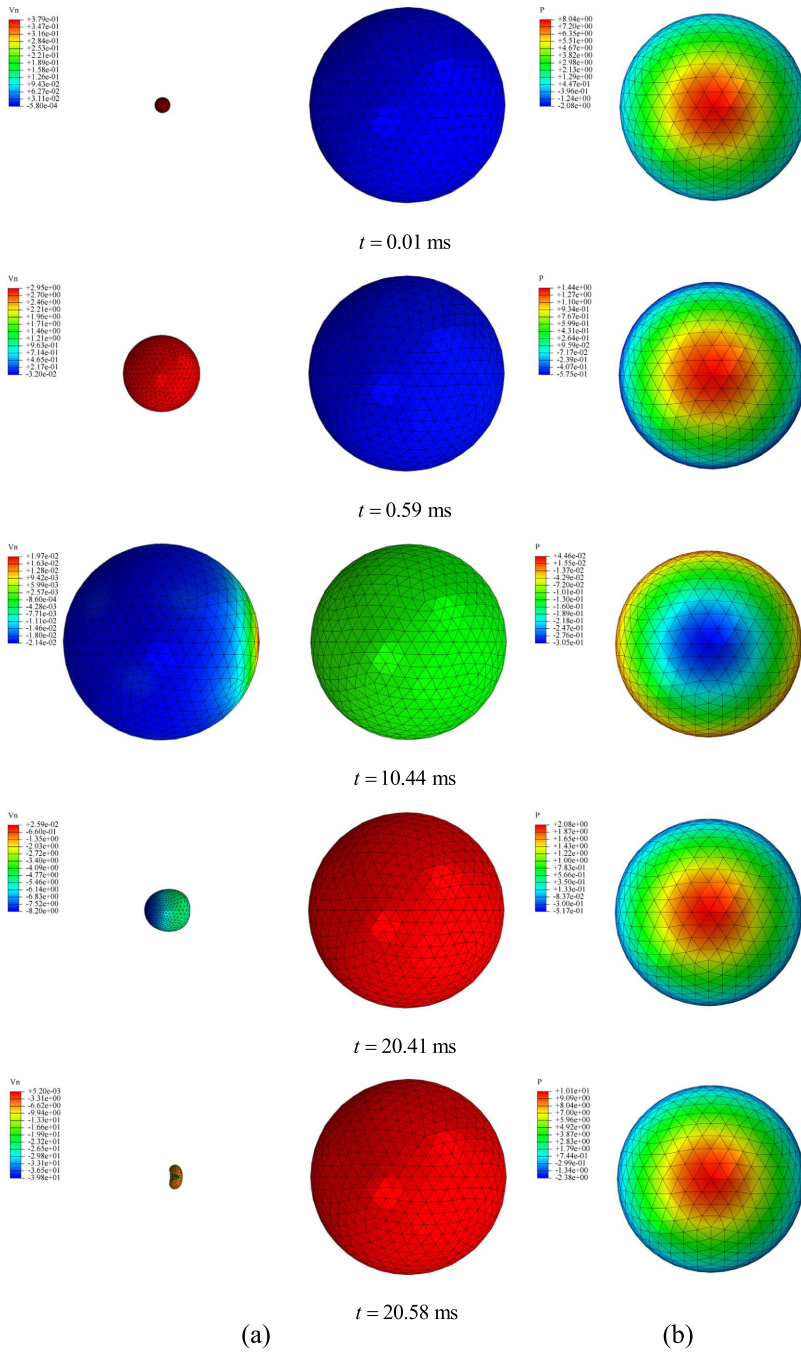(a)   (b)

FIG. 12. Interactions between a bubble (left) and an elastic sphere filled with water (right). (a) The bubble dynamic behaviors. (b) The pressure contour on the blast side of the sphere. Here, *W* = 0.4 g, *H* = 1 m, and *d* = 0.28 m. The thickness of the spherical shell is 10 mm.
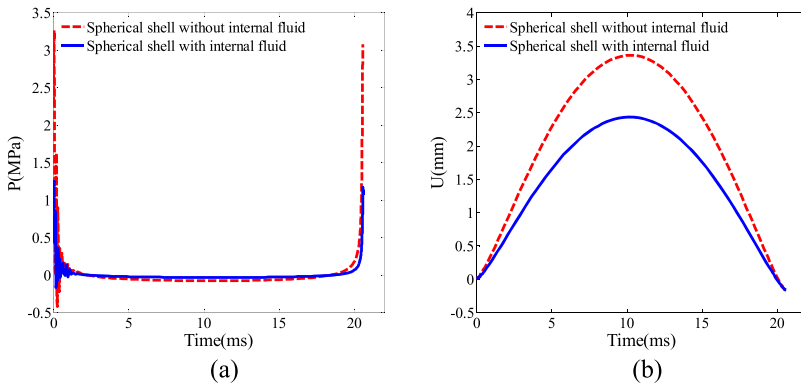

(a)   (b)

FIG. 13. Comparison of structural dynamic characteristics between a hollow sphere and a sphere with internal fluid. (a) Time evolution of the hydrodynamic pressure at the stand-off point. (b) Time evolution of the displacement at the stand-off point. *W* = 0.4 g, *H* = 1 m, and *d* = 0.28 m for two cases.
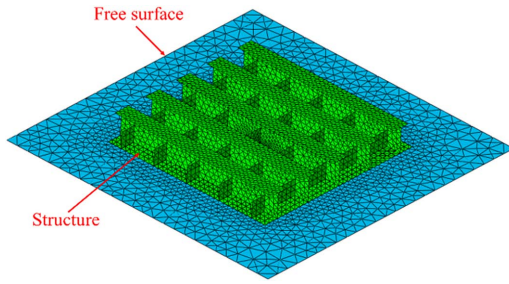
FIG. 14. Mesh generation of the model.

the charge H and the sphere are both 1 m. The initial distance between the centers of the charge and sphere d is 0.28 m. The radius of the sphere is 0.112 m. Its material properties are as follows: the mass density $\rho = 7850$ kg/m^3, Young's modulus $E = 210$ GPa, and the Poisson ratio $\upsilon = 0.3$. The thickness of the spherical shell is 10 mm. The effect of the buoyancy is ignored in this section.

For the hollow spherical shell, the hydrodynamic load acts on the outer side of the sphere, and the atmospheric pressure is the load on the inner side. However, when the spherical shell is filled with internal fluid, the hydrodynamic load acts on the two sides of the structure. At this time, the inner domain is simultaneously solved to obtain the load on the inner surface.

Figure 12(a) displays the dynamic behaviors of the bubble interacting with a sphere filled with water. Figure 12(b) displays the pressure contour on the blast side of the sphere. It shows the difference of the hydrodynamic pressure on the outer side and the inner side. The time histories of the hydrodynamic pressure and displacement of the stand-off point are shown in Fig. 13. Because the weight of the charge is small and the stiffness of the structure is strong, the coupling effect is weak in this case. After the denotation, the bubble expands and pushes the surrounding liquid outwards due to its inner high gas pressure. Meanwhile, the sphere moves away from the bubble under the influence of the fluid field environment. And a high pressure region appears on the surface of the sphere, as shown in Fig. 12(b) ($t = 0.01$ ms). With the bubble expanding, the motion of the liquid between the bubble and sphere is blocked gradually. It leads to the fact that the hydrodynamic load on the outer surface decreases and it is less than the load on the inner surface. A negative pressure region appears on the blast side of the sphere in Fig. 12(b) ($t = 10.44$ ms). The volume of the bubble and the displacement of the sphere approximately reach the maximum at this moment. Afterwards, the bubble enters the collapse phase. The inner pressure of the bubble is less than the fluid pressure and the liquid begins to rush into the bubble. In the wake of the liquid motion, the sphere is attracted by the bubble.

In order to study the influence of internal fluid on the structural dynamic behaviors, we simulate the bubble dynamics near a hollow elastic spherical shell with the same parameters. The comparison of the hydrodynamic pressure and displacement between a hollow spherical shell and a spherical shell with internal fluid is shown in Fig. 13. As shown in Fig. 13, the structural hydrodynamic load amplitude and displacement

$t = 0.52$ ms

$t = 27.65$ ms

$t = 43.66$ ms

$t = 47.52$ ms

$t = 47.89$ ms

$t = 48.48$ ms

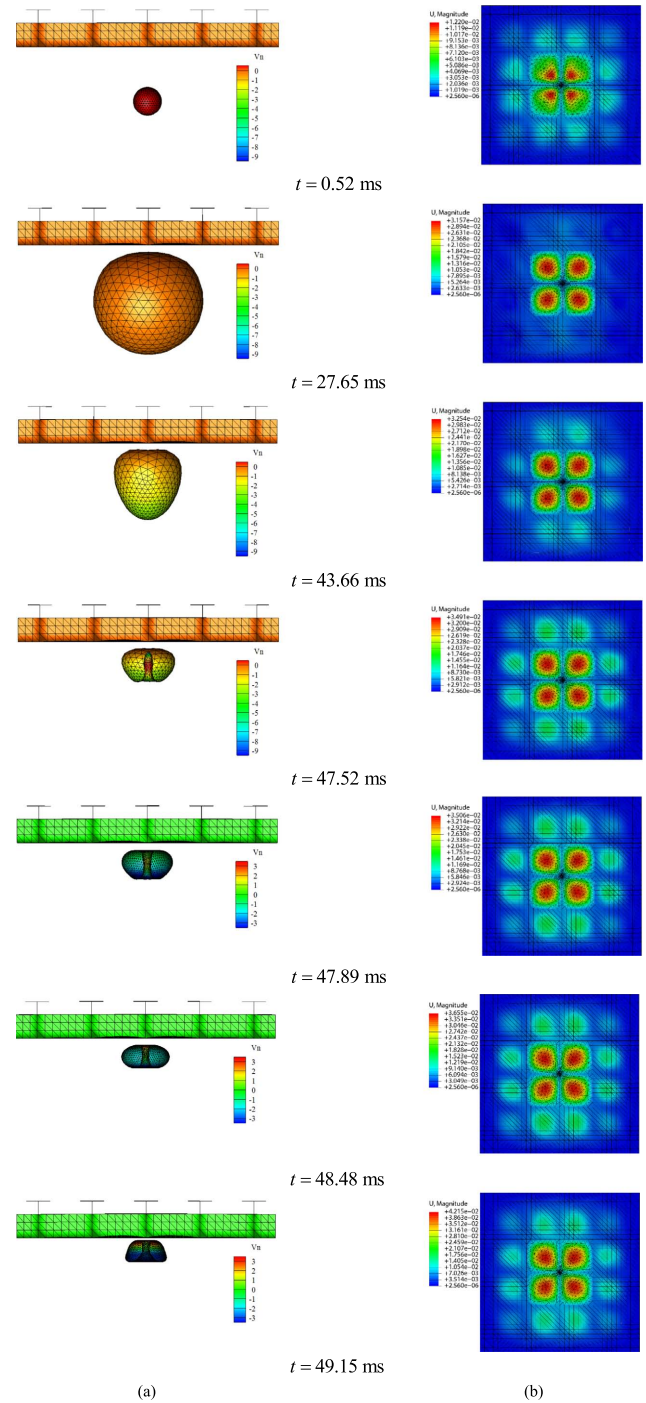$t = 49.15$ ms

(a)   (b)

FIG. 15. Evolution of bubble below an air-backed stiffened plate. (a) The bubble dynamics behaviors. (Free surface is not shown.) (b) The deformation of the bottom plating. Here, $W = 5.2$ g, $H = 0.25$ m, and the stand-off distance is 0.25 m.

amplitude decrease when the spherical shell is filled with internal fluid. It is due to the fact that the existence of the internal fluid increases the added mass of the structure. It can infer that the existence of the internal fluid is beneficial to improve the structural safety.

C. Interaction between a bubble and an air-backed stiffened structure

In this section, the interaction between a bubble and an air-backed stiffened plate is studied. Air-backed plates are
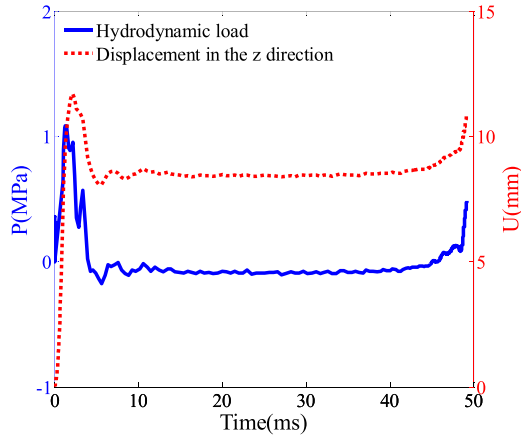
FIG. 16. Time evolution of the hydrodynamic load and displacement of the center at the panel. Here, $W = 5.2$ g, $H = 0.25$ m, and the stand-off distance is 0.25 m.

very common in the structure of the naval ship and submarine. The structure model in Sec. III is adopted again. The bottom plating is placed at the free surface. One side is air-backed, and the other side is acted by the hydrodynamic load. The edges of the bottom plating are rigidly fixed. The weight of the TNT charge is 5.2 g. The initial depth of the charge H is 0.25 m. The mesh discretization of the model is shown in Fig. 14, where the green and blue meshes denote the structure and free surface, respectively.

The dynamic boundary condition on the free surface is

$$\frac{d\phi}{dt} = \frac{|\nabla\phi|^2}{2} - g\,(z - H).\tag{30}$$

This paper mainly focuses on the coupling effect between the bubble and structure. For simplicity, the linearized free-surface condition is adopted in this section (Koo and Kim, 2004). During the whole simulation, the discretized free surface nodes are stationary, while their dynamic boundary condition (30) is updated. And the dynamic and kinematic boundary conditions on the bubble surface and wet surface are updated at each fluid time step. The bubble shape and the deformation of the bottom plating are shown in Fig. 15.

As shown in Fig. 15(b), four central panels of the bottom plating keep bulged during the whole simulation. The center of one of the panels is used to analyze the deformation of the panels. The time evolution of the hydrodynamic load and displacement of the point is shown in Fig. 16. Just after the detonation, the hydrodynamic load on the structure reaches the first peak rapidly. Due to the bubble expansion, the bottom plating is pushed by the liquid and the point moves upwards. Afterwards, the hydrodynamic load decreases and remains below the atmosphere. It makes the point move in the reverse direction. The prior generated elastic deformation is eliminated. The residual deformation is the plastic deformation. With the bubble expanding, the internal pressure of the bubble decreases gradually. When the internal pressure of the bubble is smaller than the surrounding liquid pressure, the bubble begins to collapse. In the collapse phase, different parts of the bubble have different collapsing velocities. The bubble surface, where the local curvature radius is smaller, collapses

faster (Lauterborn, 1982 and Cui *et al.*, 2016a). It leads to the fact that a narrow jet is formed at the bottom of the bubble and directs to the structure. And the hydrodynamic load reaches the second peak. The point moves upwards again under the action of the jet load.

VI. SUMMARY AND CONCLUSIONS

In this study, a new fully coupled model for the nonlinear interaction between a bubble and an elastic-plastic structure is established. The bubble dynamics and the structural transient response are solved by the boundary element method and explicit finite element method, respectively. The equations for the state variables of the fluid and structure are coupled and solved as a set of coupled linear algebra equations. Based on the acceleration potential method, the mutual dependence between the hydrodynamic load and the structural motion is decoupled, and the hydrodynamic load can be obtained accurately and directly. By comparing with the underwater explosion experiments, the numerical model shows good stability and accuracy in terms of bubble shape and structural strain response. Due to the explicit finite element structure solver, the present model can solve strongly nonlinear problems, including the material nonlinearity and geometrical nonlinearity. Thus, the model is versatile in practical applications.

We simulate the case that a bubble interacts with an elastic-plastic hollow spherical shell. By adjusting the material of the structure and the stand-off distance, the bubble shows diverse collapse and jet patterns. Interestingly, when the stiffness of the structure decreases, the coupling effect is strong and the jet would develop away from the structure. When the fully coupled model and the loosely coupled model are advanced with the same time step, the fully coupled model is more stable. With the coupling effect becoming stronger, the inaccuracy caused by non-simultaneous interaction in the loosely coupled model is enlarged. Especially, when the structure undergoes nonlinear large deformation, the coupling effect is strong nonlinear. The error of the loosely coupled model is greatly large.

The interaction between a bubble and a spherical shell filled with water is simulated. Compared with the hollow spherical shell, the structural hydrodynamic load amplitude and displacement amplitude decrease. It is due to the fact that the existence of the internal fluid increases the added mass of the structure. It can infer that the existence of the internal fluid is beneficial to improve the structural safety. Besides, in the presence of the free surface, the interaction between a bubble and an air-backed stiffened plate is simulated. The results show that the jet load is an important factor for causing damage to structures.

Belytschko, T., "A survey of numerical methods and computer programs for dynamic structural analysis," Nucl. Eng. Des. **37**, 23–34 (1976).

Belytschko, T., Stolarski, H., and Carpenter, N., "A C^0 triangular plate element with one-point quadrature," Int. J. Numer. Methods Eng. **20**, 787–802 (1984).

Best, J. P. and Kucera, A., "A numerical investigation of non-spherical rebounding bubbles," J. Fluid Mech. **245**, 137–154 (1992).

Blake, J. R. and Gibson, D. C., "Growth and collapse of a vapour cavity near a free surface," J. Fluid Mech. **111**, 123–140 (1981).

Brett, J. M. and Yiannakopolous, G., "A study of explosive effects in close proximity to a submerged cylinder," Int. J. Impact Eng. **35**, 206–225 (2008).

Chahine, G. L., Kalumuck, K. M., and Hsiao, C. T., "Simulation of surface piercing body coupled response to underwater bubble dynamics utilizing 3DYNAFS, a three-dimensional BEM code," Comput. Mech. **32**, 319–326 (2003).

Cole, R. H., *Underwater Explosions* (Princeton University Press, Princeton, USA, 1948).

Cui, P., Wang, Q. X., Wang, S. P., and Zhang, A. M., "Experimental study on interaction and coalescence of synchronized multiple bubbles," Phys. Fluids **28**, 012103 (2016a).

Cui, P., Zhang, A. M., and Wang, S. P., "Small-charge underwater explosion bubble experiments under various boundary conditions," Phys. Fluids **28**, 117103 (2016b).

Duncan, J. H., Milligan, C. D., and Zhang, S., "On the interaction between a bubble and a submerged compliant structure," J. Sound Vib. **197**, 17–44 (1996).

Flanagan, D. P. and Belytschko, T., "Simultaneous relaxation in structural dynamics," J. Eng. Mech. Div. **107**, 1039–1055 (1981).

Geers, T. L. and Hunter, K. S., "An integrated wave-effects models for an underwater explosion bubble," J. Acoust. Soc. Am. **111**, 1584–1601 (2002).

Hicks, A. N., "Explosion induced hull whipping," in *Advances in Marine Structures Conference, London* (Elsevier Applied Science Publishers, 1986), pp. 390–410.

Hsiao, C. T., Jayaprakash, A., Kapahi, A., Choi, J. K., and Chahine, G. L., "Modelling of material pitting from cavitation bubble collapse," J. Fluid Mech. **755**, 142–175 (2014).

Hsiao, C. T. and Chahine, G. L., "Dynamic response of a composite propeller blade subjected to shock and bubble pressure loading," J. Fluids Struct. **54**, 760–783 (2015).

Hughes, T. J. R., *The Finite Element Method: Linear Static and Dynamic Finite Element Analysis* (Dover, 2000).

Kim, J. H. and Shin, H. C., "Application of the ALE technique for underwater explosion analysis of a submarine liquefied oxygen tank," Ocean Eng. **35**, 812–822 (2008).

Klaseboer, E. and Khoo, B. C., "An oscillating bubble near an elastic material," J. Appl. Phys. **96**, 5808 (2004).

Klaseboer, E., Hung, K. C., Wang, C., Wang, C. W., Khoo, B. C., Boyce, P., Debono, S., and Charlier, H., "Experimental and numerical investigation of the dynamics of an underwater explosion bubble near a resilient/rigid structure," J. Fluid Mech. **537**, 387–413 (2005).

Koo, W. and Kim, M. H., "Freely floating-body simulation by a 2D fully nonlinear numerical wave tank," Ocean Eng. **31**, 2011–2046 (2004).

Lauterborn, W., "Cavitation bubble dynamics—New tools for an intricate problem," Appl. Sci. Res. **38**, 165 (1982).

Li, Z., Sun, L., and Zong, Z., "Numerical analysis of gas bubbles in close proximity to a movable or deformable body," Arch. Appl. Mech. **83**, 1715–1737 (2013).

Li, S., Han, R., and Zhang, A. M., "Nonlinear interaction between a gas bubble and a suspended sphere," J. Fluids Struct. **65**, 333–354 (2016).

Liang, C. C. and Tai, Y. S., "Shock responses of a surface ship subjected to noncontact underwater explosions," Ocean Eng. **33**, 748–772 (2006).

Liu, Y. L., Wang, Q. X., Wang, S. P., and Zhang, A. M., "The motion of a 3D toroidal bubble and its interaction with a free surface near an inclined boundary," Phys. Fluids **28**, 122101 (2016a).

Liu, Y. L., Wang, S. P., and Zhang, A. M., "Interaction between bubble and air-backed plate with circular hole," Phys. Fluids **28**, 062105 (2016b).

Liu, N. N., Cui, P., Ren, S. F., and Zhang, A. M., "Study on the interactions between two identical oscillation bubbles and a free surface in a tank," Phys. Fluids **29**, 052104 (2017).

Ming, F. R., Zhang, A. M., Xue, Y. Z., and Wang, S. P., "Damage characteristics of ship structures subjected to shockwaves of underwater contact explosions," Ocean Eng. **117**, 359–382 (2016).

Rungsiyaphornrat, S., Klaseboer, E., Khoo, B. C., and Yeo, K. S., "The merging of two gaseous bubbles with an application to underwater explosions," Comput. Fluids **32**, 1049–1074 (2003).

Sprague, M. A. and Geers, T. L., "A spectral-element/finite-element analysis of a ship-like structure subjected to an underwater explosion," Comput. Methods Appl. Mech. **195**, 2149–2167 (2006).

Tanizawa, K., "A nonlinear simulation method of 3-D body motions in waves (1st report)," J. Soc. Nav. Archit. Jpn. **178**, 179–191 (1995).

Turangan, C. K., Ong, G. P., Klaseboer, E., and Khoo, B. C., "Experimental and numerical study of transient bubble-elastic membrane interaction," J. Appl. Phys. **100**, 054910 (2006).

Van Daalen, E. F. G., "Numerical and theoretical studies of water waves and floating bodies," Ph.D. thesis, University of Twente, 1993.

Vinje, T. and Brevig, P., "Numerical simulation of breaking waves," Adv. Water Resour. **4**, 77–82 (1981).

Wang, Q. X., Yeo, K. S., Khoo, B. C., and Lam, K. Y., "Nonlinear interaction between gas bubble and free surface," Comput. Fluids **25**, 607–628 (1996).

Wang, Q. X., "The evolution of a gas bubble near an inclined wall," Theor. Comput. Fluid Dyn. **12**, 29–51 (1998).

Wang, C. and Khoo, B. C., "An indirect boundary element method for three-dimensional explosion bubbles," J. Comput. Phys. **194**, 451–480 (2004).

Wang, Q. X., Yeo, K. S., Khoo, B. C., and Lam, K. Y., "Vortex ring modelling of toroidal bubbles," Theor. Comput. Fluid Dyn. **19**, 303–317 (2005).

Wu, G. X. and Hu, Z. Z., "Simulation of nonlinear interactions between waves and floating bodies through a finite-element-based numerical tank," Proc. R. Soc. A **460**, 2797–2817 (2004).

Zhang, N. and Zong, Z., "Hydro-elastic-plastic dynamic response of a ship hull girder subjected to an underwater bubble," Mar. Struct. **29**, 177–197 (2012).

Zhang, A. M., Li, S., and Cui, J., "Study on splitting of a toroidal bubble near a rigid boundary," Phys. Fluids **27**, 062102 (2015).

Zhang, A. M. and Liu, Y. L., "Improved three-dimensional bubble dynamics model based on boundary element method," J. Comput. Phys. **294**, 208–223 (2015).

Zhang, A. M., Sun, P. N., Ming, F. R., and Colagrossi, A., "Smoothed particle hydrodynamics and its applications in fluid-structure interactions," J. Hydrodyn., Ser. B **29**, 187–216 (2017).

Zienkiewicz, O. C., Taylor, R. L., and Zhu, J. Z., *The Finite Element Method: Its Basis and Fundamentals*, 7th ed. (Butterworth-Heinemann, 2013).

Zong, Z., "A hydroplastic analysis of a free–free beam floating on water subjected to an underwater bubble," J. Fluids Struct. **20**, 359–372 (2005).

Zong, Z., Wang, J. X., Zhou, L., and Zhang, G. Y., "Fully nonlinear 3D interaction of bubble dynamics and a submerged or floating structure," Appl. Ocean Res. **53**, 236–249 (2015).